Nano and micro reoriented domains and their relation with the crystal structure in the new ferroelectric boracite $Zn_3B_7O_{13}Br$

2006 J. Phys.: Condens. Matter 18 4827

(http://iopscience.iop.org/0953-8984/18/20/007)

INSTITUTE OF PHYSICS PUBLISHING JOURNAL OF PHYSICS: CONDENSED MATTER

J. Phys.: Condens. Matter **18** (2006) 4827–4837 doi:10.1088/0953-8984/18/20/007

Nano and micro reoriented domains and their relation with the crystal structure in the new ferroelectric boracite $Zn_3B_7O_{13}Br$

J Campa-Molina[1], S Ulloa-Godínez[1], A Barrera[1], L Bucio[2] and J Mata[3]

[1] Centro Universitario de la Ciénega, Universidad de Guadalajara, Laboratorio de Materiales, Avenida Universidad No. 1115, Colonia Linda Vista, CP 47840, Ocotlán, Jalisco, Mexico
[2] Instituto de Física, UNAM, Apartado Postal 20-364, 01000 México, DF, Mexico
[3] Centro de Ciencias de la Materia Condensada, UNAM, Apartado Postal 2681, E-22800, Ensenada, BC, Mexico

Received 26 January 2006, in final form 10 April 2006
Published 2 May 2006
Online at stacks.iop.org/JPhysCM/18/4827

Abstract

A new zinc brome boracite $Zn_3B_7O_{13}Br$ has been grown by a chemical transport reaction in closed quartz ampoules at 920 K. The crystal structure was characterized by Rietveld refinement. Ferroelectric nano and micro reorientable domains were found in this material using polarizing optical microscopy (PLM), scanning electron microscopy (SEM) and transmission electron microscopy (TEM). Chemical analysis was performed with x-ray energy dispersive spectroscopy (EDX). In the crystal, a new structure transition at 586 K from orthorhombic ($Pca2_1$) to cubic cell ($F\bar{4}3c$) has been found. This transition was corroborated by differential scanning calorimetry (DSC).

(Some figures in this article are in colour only in the electronic version)

1. Introduction

The new zinc brome boracite $Zn_3B_7O_{13}Br$ (henceforth abbreviated as Zn–Br) belongs to the family with the general formula $Me_3B_7O_{13}X$, where Me could be a divalent ion (Mg, Cr, Mn, Fe, Co, Ni, Cu, Zn or Cd) and X a halogen (Cl, Br or I). Occasionally, X could be OH, S, Se, Te or F. The origin of the term 'boracite' is due to the mineral $Mg_3B_7O_{13}Cl$; this term is given, at present, to more than 25 isomorphous compound [1–6].

Boracites have attracted the attention of researchers since Häuy (1791), who observed pyroelectricity in the mineral boracite $Mg_3B_7O_{13}Cl$ [1]. At the end of the 19th century, the phenomenon of pyroelectricity was studied by Hankel, Jacques and Pierre Curie [2]. In the 1970s, the study of boracite arose again because of its interesting physical properties, some with a controversial origin; for example, after more than 30 years of discussion, in 1964 Ascher [3–5] gave an indisputable demonstration of ferroelectricity, i.e. the inversion and/or reorientation of the spontaneous polarization by means of an external applied electric field. In 1966 Asher also

proved the ferromagnetoelectric effect, i.e. the coexistence of a spontaneous polarization and spontaneous magnetization at low temperatures [6].

Nowadays, boracites have received special attention because of their unusual physical properties, which make them have potential applications: an optic stopper due to the modification in birefringence produced by the application of a mechanical strain, electric field, electron beam and/or temperature change [7]; ferroelectric nonvolatile memory (ferroelectric random access memory, or FRAM) because of the reorientation of its ferroelectric domains [8]; and infrared (IR) detection due to the intrinsic pyroelectricity of the boracite [9, 10]. One characteristic that makes these boracites unique is the ferroelectricity phenomenon (domain reorientation) which can be observed using almost any microscopy technique, while, in most of the ferroelectric compounds, the ferroelectricity is confirmed just with a hysteresis cycle [9, 10].

The Zn–Br boracite transformed from a cubic high-temperature phase (point group $\overline{4}3m$) to an orthorhombic low-temperature phase ($m2m$) at 586 K. Phase transitions accompanied by a change of the point-group symmetry are generally called ferroic [11]. A ferroic crystal contains two or more possible orientation states or domains; under a suitably chosen driving force, the domain walls (the intermediate regions between domains) move, switching the crystal from one domain to another [12]. The formation of domains is a normal phenomenon that occurs during non-destructive ferroic phase transitions, involving symmetry reduction, usually upon cooling from the high-temperature phase. In such a case, the twinning laws of the ferroic phase, i.e. the symmetry operations to transform one domain into all others, are given by the symmetry elements that are lost during the transition [13–16]. The study of domain structures is important for understanding the properties of ferroelectric materials, because their properties are determined by domain structures [17]. To our knowledge, very few attempts have been made to correlate the physical properties of boracites to their domain structures [18], but none have tried to correlate ferroelectric domains with crystal structure. The existence of domains is well known, although nano-domains have never been reported.

The aim of this work is to characterize the domain structure in the orthorhombic phase of Zn–Br (using PLM, SEM and TEM) and to relate it to its crystal structure.

2. Experimental details

Colourless single crystals of Zn–Br were grown by a chemical vapour transport technique, commonly called the three-crucibles method, reported by Schmid [19]. Growth takes place in a closed quartz ampoule. Chemical transport reactions were carried out by heating the ampoule at about 1193 K in a resistance-heated vertical furnace, with gradients of 850 K (above) and 650 K (below), over a period of 72 h. The reactants were placed in the following order: B_2O_3, which was obtained by dehydrating H_3BO_3, was placed in the first crucible; ZnO in the second crucible; and $ZnBr_2$ in the third crucible. Zn–Br crystals as large as 2 mm in size were commonly obtained.

An unusual problem arising in the study of boracites is that presented by the phenomenon of 'growth sectors'. Crystal growth in the cubic phase proceeds at different rates along ⟨100⟩, ⟨110⟩ and ⟨111⟩ [20]; this is shown figure 1.

For PLM and SEM work, platelets were cut from as-grown crystals parallel to a naturally formed cubic (100) facet for Zn–Br; this is shown in figure 1. For PLM, the opposite surface of the specimen was finally polished to optical quality by using diamond paste of 0.7 μm grain size. The surfaces of Zn–Br were not metallized. The typical sample thickness was 60 μm and the area ranged up to 0.014 cm^2. The observed Zn–Br sample was freely mounted on the rotary stage of a polarizing light microscope (Leitz Ortoplan Pol). For SEM, the same uncoated sample was attached to a brass cylindrical holder with a carbon paint. This holder was mounted

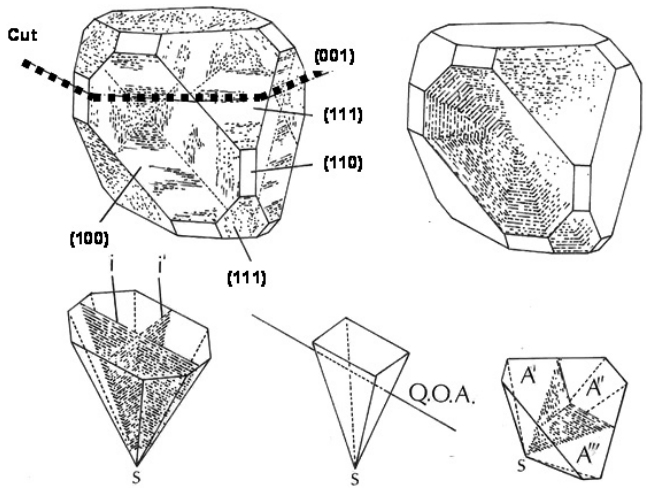

Figure 1. Crystal growth in the cubic phase proceeds at different rates along ⟨100⟩, ⟨110⟩ and ⟨111⟩. The resulting growth, or sector, usually occurs together in the one 'single' crystal, which exhibits different optical properties [20]. Platelets were cut from as-grown crystals parallel to a naturally formed cubic (100) facet.

in a JEOL SEM 5200 microscope with a NORAN-EDX instrument. For TEM, the sample was crushed in a mortar and suspended in alcohol. A drop of the solution was put on a specimen grid covered by a thin holey carbon film. The sample was mounted on the stages of a JEOL STEM 100-CX.

In order to perform single-crystal x-ray diffraction analysis, a good-quality crystal is necessary, but the micro-domains can be easily confused with micro-twins, causing cdifficulty in selection. Therefore, we decided to use x-ray powder diffraction and Rietveld refinement methods.

The x-ray powder diffraction (XRD) pattern was recorded at room temperature in a Siemens D5000 diffractometer with a vertical goniometer. A fixed diffracted beam graphite monochromator and scintillation counter were used. A Cu Kα anode operating at 40 kV and 25 mA was used. The 2θ-range was 12°–90°, with 0.02° step size and 10 s counting time.

The Rietveld method, implemented in the program FULLPROF [21], was used to refine the crystal structure. A pseudo-Voigt function modified by Thompson *et al* [22] was chosen to generate the shape of the diffraction peaks. The following parameters were refined: zero point, scale factor, linear interpolation between 32 fixed points for the background, unit cell dimensions, half-width, pseudo-Voigt and asymmetry parameters for the peak shape; position, thermal isotropic factors and occupation numbers for Zn and Br atoms.

3. Results and discussion

3.1. Structural characterization

The lattice parameters and the space group, determined by x-ray precession method, were $a = 8.56$ Å, $b = 8.55$ Å, and $c = 12.10$ Å with $\alpha = \beta = \gamma = 90°$ and orthorhombic spacial group $Pca2_1$. This unit cell and the ratios between their lattice parameters were compatible with the unit cell exhibited by the $Fe_3B_7O_{13}I$ boracite compound, whose symmetry is described by the space group $Pca2_1$ (No. 29) and reported by Kubel and Janner [23].

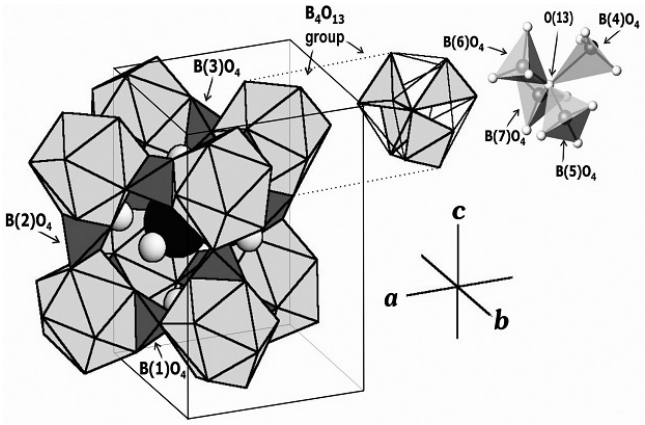

Figure 2. Crystal structure of Zn–Br boracite. The boron tetrahedrals which form the B_4O_{13} groups and which were fixed as a rigid body ($B(1)O_4$, $B(2)O_4$ and $B(3)O_4$) can be seen.

Initial refinement gave relatively high values of $\chi^2 = 12.6$ and $R_B = 8.4$, where [24]:

$$\chi = \frac{R_{wp}}{R_e} = S$$

where $S =$ (The '*Goodness of fit*' indicator), $R_{wp} =$ (R-weighted pattern), $R_e =$ (R-expected), and $R_B =$ (R-Bragg factor).

In order to reduce these high values, we tried to refine the boron coordinates, but rigid-body constraints had to be applied because of the complexity of the structure model and boron's intrinsic dispersive limitations. Hence, in figure 2, three rigid-body definitions for the tetrahedral BO_4 were employed.

The three defined rigid bodies ($B(1)O_4$, $B(2)O_4$ and $B(3)O_4$) had their origin at the B atom. The tetrahedrals that do not share oxygen atoms were not fixed, in order to allow movement in the model. Consequently, the boron tetrahedral that forms the B_4O_{13} groups was not fixed as a rigid body. The use of the above rigid bodies reduced, significantly, the number of positional parameters in Rietveld refinement. At this stage, the refinement successfully proceeded and ended with reasonable merit figure values of $\chi^2 = 6.03$ and $R_B = 4.03$. The experimental, calculated, and difference in x-ray diffraction patterns of Zn–Br are plotted in figure 3.

The structural parameters determined from x-ray powder diffraction data at room temperature are summarized in table 1; the final refined positional and thermal parameters are given in table 2; the main interatomic distances are given in table 3.

The bond distance values of table 3, on first approach, look mistaken, because the difference between the coordination polyhedral bond distance values is too big. For example, the octahedral polyhedral, whose central atoms are Zn, is coordinated with two bromines and four oxygens; the average bond distances Zn–Br and Zn–Br′ are 3.39 and 2.66 Å, which implies a big distortion in the polyhedron. This polyhedral distortion is characteristic of every boracite compound [3, 6, 22, 25, 26]. Although the polyhedral distortion is evident, the Zn–Br unit cell is symmetrical, showing a pseudo-cubic $[100]_{cub}$ symmetry. Using Pythagoras's relation ($d = \sqrt{a^2 + b^2}$), we found that the diagonal value between the lattice constant a and b is 12.097 Å, which is almost the same value of the c parameter (12.0998 Å), confirming the pseudo-cubic $[100]_{cub}$ symmetry (figure 4(A)). Of the three lengths a, b and c, b is the shortest in Zn–Br [$b = 8.5492(2)$]; it is one half of the length of the pseudo-cubic face diagonal $[110]_{cub}$. This means that squeezing a crystal plate of Zn–Br along a pseudo-cubic $[110]_{cub}$

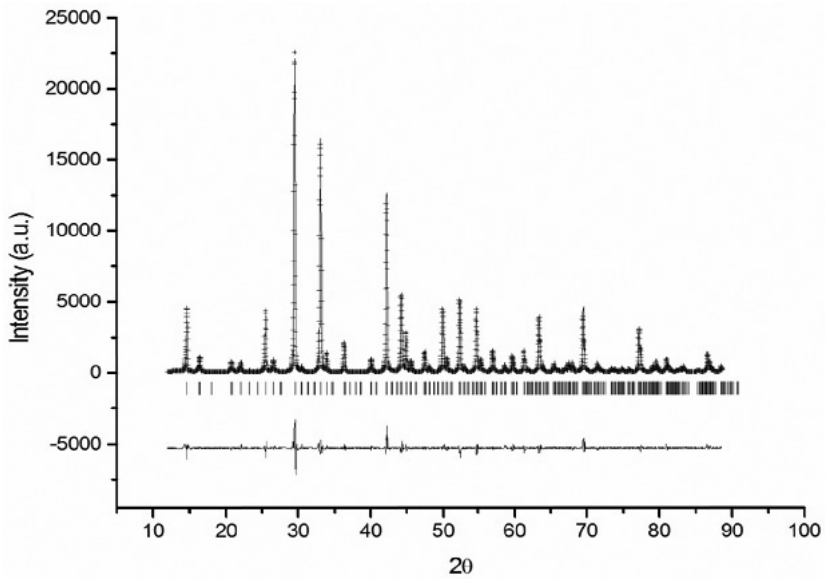

Figure 3. The observed (crosses), calculated (solid line) and difference (at the bottom) x-ray powder diffraction profiles for Zn–Br at room temperature. Vertical marks correspond to the position of the allowed Bragg reflections.

Table 1. Lattice parameters and discrepancy factors for $Zn_3B_7O_{13}Br$; space group $Pca2_1$ (No. 29).

Lattice parameters	
a (Å)	8.5506(2)
b (Å)	8.5599(2)
c (Å)	12.0994(2)
Vol. (Å^3)	885.58(3)
Reliability factors (%)	
R_P	8.44
R_{exp}	4.63
S	2.45
R_{Bragg}	4.03
R_F	3.24

direction may lead, under favourable conditions, to a single domain with the b axis along the squeezing direction. Moreover, the preferential orientation in Rietveld refinement is along the $[111]_{orth}$ or $[110]_{cub}$ directions.

In the boracite Zn–Br crystal structure, as we mentioned before, strong deformations in the tetrahedral BO_4 and octahedral $BrZn_6$ polyhedra can be seen. These deformations provoke the total atom charge in the crystal structure not to be neutralized; consequently, zones with negative and positive charge appear. In other words, the distortion generates electric dipoles along the crystal structure preferably along the $[111]_{orth}$ or $[110]_{cub}$ directions.

All halogen boracites exhibit a high-temperature cubic phase symmetry $F\bar{4}3c$ (No. 219). Figure 4(A) clearly shows the boracite Zn–Br phase transition from cubic into a polar orthorhombic $Pca2_1$ (No. 29) phase at 586 K; the DSC result is displayed in figure 4(B). The change from the cubic phase to the orthorhombic phase involves brome displacement, taken

Table 2. Final refined positional and thermal parameters for $Zn_3B_7O_{13}Br$ at room temperature are shown; space group $Pca2_1$ (No. 29).

Atom	*X*	*Y*	*Z*	*B* (Å^2)
Br	0.7628(4)	0.2504(8)	0.521(6)	0.80(9)
Zn(1)	0.7580(6)	0.247(1)	0.236(1)	0.62(6)
Zn(2)	0.4906(8)	0.528(1)	0.515(6)	0.62(6)
Zn(3)	−0.0152(8)	0.029(1)	0.511(6)	0.62(6)
B(1)	0.496(2)	0.508(2)	0.773(6)	0.165
B(2)	0.260(1)	0.247(2)	0.528(6)	0.165
B(3)	0.004(3)	−0.016(2)	0.272(6)	0.165
B(4)	0.420(4)	0.251(8)	0.412(6)	0.165
B(5)	0.205(6)	0.285(1)	0.200(7)	0.165
B(6)	0.887(6)	0.76(1)	0.859(7)	0.165
B(7)	0.7579	0.9054	0.6776	0.165
O(1)	0.230(3)	0.251(6)	0.268(6)	0
O(2)	0.541(2)	0.344(2)	0.294(6)	0
O(3)	0.383(1)	0.333(2)	0.463(6)	0
O(4)	−0.028(3)	0.258(2)	0.285(6)	0
O(5)	0.177(1)	0.365(2)	0.594(6)	0
O(6)	0.175(3)	−0.032(2)	0.247(6)	0
O(7)	0.142(1)	0.173(2)	0.453(6)	0
O(8)	0.334(2)	0.536(2)	0.253(6)	0
O(9)	0.333(1)	0.127(2)	0.593(6)	0
O(10)	0.550(2)	0.604(2)	0.369(6)	0
O(11)	−0.034(2)	−0.092(2)	0.371(6)	0
O(12)	0.588(2)	0.558(2)	0.172(6)	0
O(13)	−0.080(3)	−0.064(2)	0.170(6)	0

Table 3. Main bond distances (Å) of $Zn_3B_7O_{13}Br$ at room temperature.

Octahedral configurations							
Zn(1)–Br	3.45(9)	Zn(2)–Br	3.36(1)	Zn(3)–Br	3.36(1)	Br–Zn(1)	3.45(9)
Br′	2.61(9)	Br′	2.70(1)	Br′	2.68(1)	Zn(1)	2.61(9)
O	2.13(4)	O	2.03(9)	O	2.01(4)	Zn(2)	3.36(1)
O	1.96(2)	O	2.06(9)	O	2.05(4)	Zn(2)	2.70(1)
O	2.04(3)	O	2.03(4)	O	2.08(9)	Zn(3)	2.68(1)
O	1.98(2)	O	2.04(4)	O	2.01(9)	Zn(3)	3.36(1)
Tetrahedral configurations							
B(1)–O(2)	1.34(3)	B(2)–O(3)	1.51(5)	B(3)–O(4)	1.53(2)	B(4)–O(1)	2.39(8)
O(8)	1.48(3)	O(5)	1.47(5)	O(6)	1.50(4)	O(2)	1.94(8)
O(10)	1.57(8)	O(7)	1.49(6)	O(11)	1.40(9)	O(3)	0.99(8)
O(12)	1.54(8)	O(9)	1.46(6)	O(13)	1.48(9)	O(11)	1.50(7)
B(5)–O(1)	0.9(1)	B(6)–O(1)	1.49(9)	B(7)–O(1)	1.73(6)		
O(5)	1.77(8)	O(4)	1.67(8)	O(6)	1.48(5)		
O(8)	2.50(6)	O(7)	1.3(1)	O(9)	1.24(6)		
O(12)	1.90(8)	O(10)	1.43(8)	O(13)	1.54(2)		

with respect to the cubic positions as reference: one in the middle of them, parallel to the triple axis [111], and the other one in the middle parallel to the $[\bar{1}\bar{1}\bar{1}]$ direction (figure 5). The zinc ion displacements are parallel to the cubic directions $[100]_{cub}$. Zinc and brome displacements

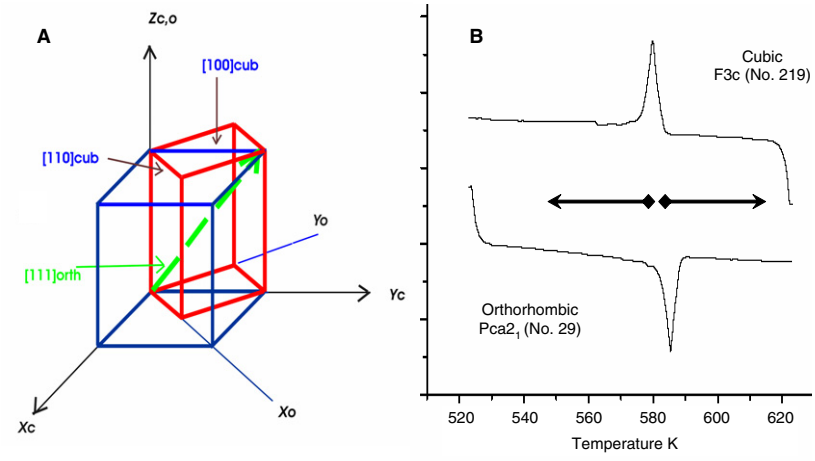

Figure 4. (A) Relation between the Zn–Br orthorhombic and pseudo-cubic unit cell, as in [27]. (B) Zn–Br phase transitions from cubic to orthorhombic symmetry at 586 K (DSC).

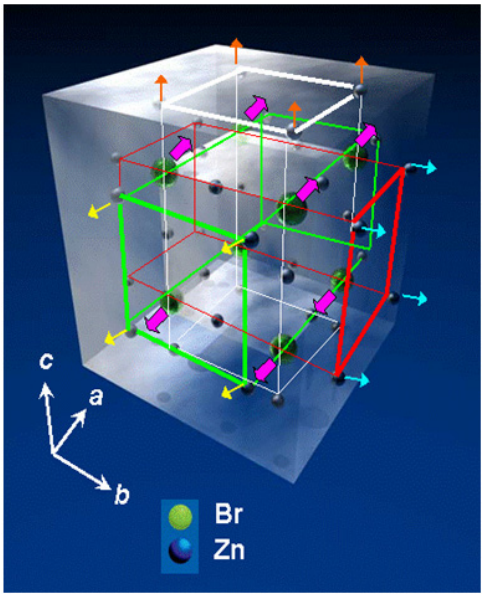

Figure 5. Zinc and brome sub-network in the boracite. Changes from the cubic phase to the orthorhombic phase involving boron displacement are indicated by arrows, as in [27].

allow us to identify three sub-nets that are mutually perpendicular; the combination of all zinc and brome displacements generate electric dipoles along the $[111]_{orth}$ or $[110]_{cub}$ directions.

Although we describe the electric dipole formation just in terms of zinc and brome displacements, Dowty and Clark [28] showed that the oxygen–boron displacements have important contributions to the spontaneous polarization.

The temperature change in the boracites has a direct effect on modification of the electric dipole moment. In general, when a pyroelectric crystal is heated, two results can be expected: (a) polarization changes with form and volume constant; (b) polarization changes with a free

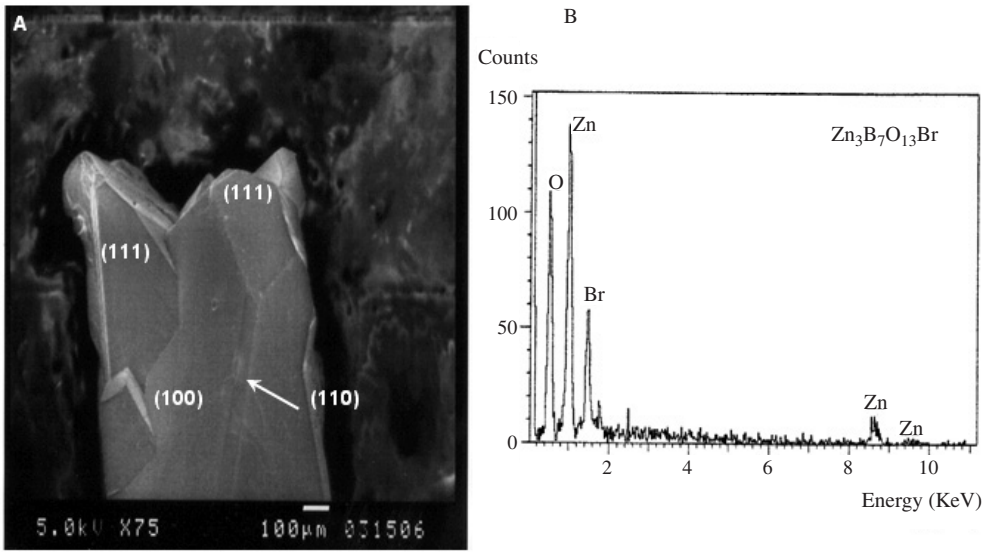

Figure 6. (A) SEM image: a general view of the synthesized crystals for the Zn–Br system. These sectors are typical in crystals like boracites, as shown in figure 1. (B) Semi-quantitative EDX spectrum from the crystals.

crystal deformation. In the first case, the phenomenon is called the true pyroelectric effect; in the second case, the phenomenon is called the false pyroelectric effect (piezoelectric case).

In figure 6(A), a general view of the crystals obtained is shown. The crystals are very well formed; typical crystal morphology is clearly exhibited and their size is in the range 1–2 mm. Schmid has shown that crystal growth in the cubic phase proceeds at different rates along ⟨100⟩, ⟨111⟩ and ⟨110⟩ [20]. A semi-quantitative EDX spectrum from the crystal is shown in figure 6(B). This spectrum indicates the presence of zinc, bromine and oxygen in the crystals (17.72, 5.63, 76.74 at.%, respectively); the boron percentage was determined from the stoichiometry (39.41 at.%). These percentages indicate an approximate chemical formula for the new compound very close to $Zn_3B_7O_{13}Br$.

According to group theory and structural considerations, the low-symmetry phases in boracites are fully ferroelectric/fully ferroelastic, i.e. an electric field and/or a stress field have full command over all possible ferroelectric and ferroelastic domain states. The symmetry properties of these ferroic species are unique, in that they allow optical contrast between all of the possible domain states. So, examination by means of the polarizing microscope is the most direct method for revealing the static domain structure, because the polarization vector Ps and optical indicatrix are oriented differently in every domain.

Observing a $(001)_{cub}$ cut of Zn–Br single crystals of boracites, large domains can be seen. They appear mainly as stripes directed along $[110]_{cub}$ or $[1\bar{1}0]_{cub}$ (figure 7(A)), although a great number of them show complicated lamellar configurations. Besides, sometimes it is difficult to distinguish between micro-domains and micro-twins.

Regarding the application of SEM for revealing the domain structure in ferroelectric materials, Le Bihan has developed a theoretical model of the charging mechanism of an insulating sample irradiated by an electron beam [29]. According to this model, accelerating voltages of a few kiloVolts generate equilibrium between the electrons impinging and leaving the surface of the sample, which stops the specimen from charging up, thus allowing domains in ferroelectric crystals to be observed.

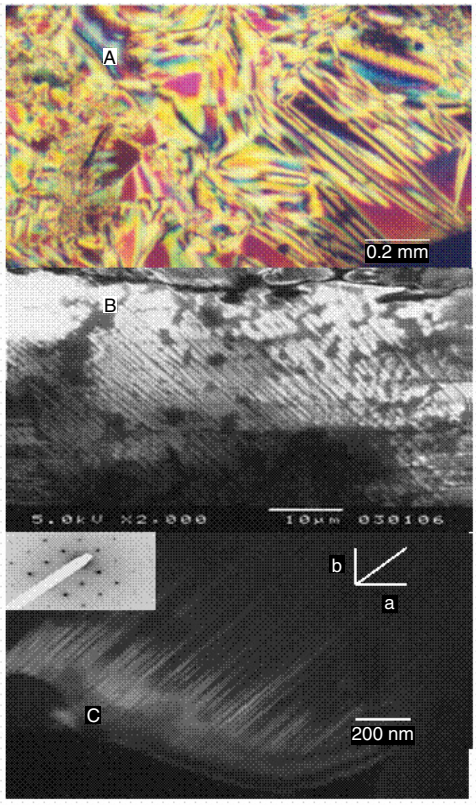

Figure 7. (A) Domain structure on a $(001)_{cub}$ Zn–Br platelet at room temperature. The PLM image shows strongly birefringent lamellae oriented approximately along $[110]_{cub}$. (B) Micro-domain structure of Zn–Br boracite, as observed by SEM. The micro-domain structures are parallel to (001). (C) TEM dark-field image of spike-like nano-domains are oriented along $[100]_{cub}$ in Zn–Br boracite. The lamellae nano-domains are parallel to (110). The incident electron beam is closely parallel to [100].

When observing domains in ferroelectric crystals, it has been shown that positive ends of domains appear dark compared to negative ends. This contrast is due to the difference in potential between domains of opposite polarity induced by spontaneous polarization (figure 7(B)). In our experiments, when the application of an accelerating voltage is <10.0 keV the domains can be reoriented several times, but when it is >10.0 keV the domain orientation is permanent. In our experiment, the application of an accelerating voltage of 0.5 kV was required to reveal the micro-domain structure in Zn–Br boracite.

Using TEM in dark-field mode, we can identify spike-like nano-domain structures (figure 7(C)). Thin (30–50 nm) mostly planar domains were parallel to (110) and oriented along $[100]_{cub}$ in Zn–Br boracite. The domains are due to the loss of symmetry at the ferroic transition from cubic ($F\bar{4}3c$ No. 219) to orthorhombic ($Pca2_1$ No. 29) symmetry. Each of these domains has one of the six possible orthorhombic orientations. Since the orthorhombic structure is still pseudo-cubic, the domains can be seen as being in a pseudo-merohedral twin relationship. In order to confirm that the nano-domains in figure 7(C) are not produced by a twin effect, in figure 6 the insets show an electron diffraction pattern of the sample that confirms it is a single crystal.

4. Summary

$Zn_3B_7O_{13}Br$ (Zn–Br) boracite was synthesized by the vapour transport method. The compound crystallizes in the orthorhombic system with the space group $Pca2_1$ (No. 29) and cell parameters $a = 8.5506(2)$, $b = 8.5599(2)$, and $c = 12.0994(2)$ Å, and Vol. $= 885.58(3)$ Å^3. A crystal structure transition from orthorhombic (No. 29), at 586 K, to cubic cell $F\bar{4}3c$ (No. 219) has been found. Although the Zn–Br orthorhombic unit cell is symmetrical, showing a pseudo-cubic $[100]_{cub}$ symmetry, the polyhedra show a remarkable distortion. The polyhedral distortion and the crystal squeezing along the pseudo-cubic $[110]_{cub}$ direction promote domain formation. In other words, the distortion generates electric dipoles along the crystal structure preferably along the $[111]_{orth}$ or $[110]_{cub}$ directions. From Rietveld refinement, we found a preferential orientation along the $[111]_{orth}$ direction.

Nano and micro ferroelectric domains were observed in this material using PLM, SEM and TEM. In just a few materials, ferroelectric domains can be seen; in this Zn–Br material, the domains can be observed even on the nano-scale.

Acknowledgments

The authors wish to express their thanks to D Argott de Juarez for her technical assistance. They also thank the Microscopy Central Laboratory (LCM-IFUNAM, México) and the Institut für Geowissenschaften (Universität Kiel, Germany). J Campa-Molina would like to thank DAAD-Germany for a sandwich Stipendium.

References

[1] Dana J D 1951 *Dana's System of Mineralogy* ed C Palache, H Berman and C Frondel (New York: Wiley)
[2] Curie P and Curie J 1880 *C. R. Acad. Sci.* **91** 294
[3] Ascher E, Schmid H and Tar D 1964 *Solid State Commun.* **2** 45
[4] Le Corre Y 1957 *J. Phys. Radium* **18** 629
[5] Sonin A S and Zheludev I S 1963 *Sov. Phys.—Crystallogr.* **8** 217
[6] Ascher E, Rieder H, Schmid H and Stössel H 1966 *J. Appl. Phys.* **37** 1404
[7] Smart L and Moore E 1992 *Solid State Chemistry, An Introduction* (London: Chapman and Hall)
[8] Mathews S, Ramesh R, Venkatesan T and Benedetto J 1997 *Science* **276** 238
[9] Campa-Molina J and Castellanos-Guzman A G 1994 *Solid State Commun.* **89** 963
[10] Campa-Molina J, Blanco O, Correa-Gomez A, Czank M and Castellanos-Guzman A G 2002 *J. Microsc.* **208** 201
[11] Wadhawan V K 2000 *Introduction to Ferroic Materials* (New York: Gordon and Breach) pp 189–215
[12] Aizu K 1970 *Phys. Rev.* B **2** 754
[13] Schmid H 1992 Polarized light microscopy (PLM) of ferroelectric and ferroelastic domains in transmitted and reflected light *Ferroelectric Ceramics* ed N Setter (Basel: Monte Verità, Birkhäusen Verlag)
[14] Salje E H K 1993 *Phase Transitions in Ferroelastic and Coelastic Crystals* (Cambridge: Cambridge University Press) pp 1–8
[15] Fousek J 1980 Some aspects of domain structures in ferroics *Applications of Ferroelectrics (Erice, Sicily, 1980)* (*Int. Summer School on Materials Science and Technology, Lecture Notes, 1st Course*)
[16] Wadhawan V K 1998 *Phase Transit.* **64** 165
[17] Cao W and Cross L E 1994 *Ferroelectrics* **157** 19
[18] Burzo E 1993 Boracites $Me_3B_7O_{13}X$ and related compounds *Numerical Data and Functional Relationships in Science and Technology* (*Landolt–Börnstein, New Series* Group III, vol 27h) (Berlin: Springer) pp 128–204
[19] Schmid H 1965 *J. Phys. Chem. Solids* **26** 973
[20] Schmid H 1969 Twinning and sector growth in nickel boracites grown by transport reactions *Growth of Crystals* vol 7 (New York: Consultants Bureau) pp 25–52 (Translated from Russian)
[21] Rodríguez-Carvajal J 1981 FULLPROF program for Rietveld refinement and pattern matching analysis (unpublished). The program is a strongly modified version of that described by D B Wiles, R A Young *J. Appl. Crystallogr.* **14** 149

[22] Thompson P, Cox D E and Hastings J B 1987 *J. Appl. Crystallogr.* **20** 79
[23] Kubel F and Janner A M 1993 *Acta Crystallogr.* C **49** 657
[24] Young R A 1996 *The Rietveld Method, IUCr Monographs on Crystallography* (Oxford: Oxford Science Publications)
[25] Kubel F, Mao S Y and Schmid H 1992 *Acta Crystallogr.* C **48** 1167
[26] Ito T, Morimoto N and Sadanaga R 1951 *Acta Crystallogr.* **4** 310
[27] Tolédano P, Schmid H, Clin M and Rivera J P 1985 *Phys. Rev.* B **32** 6006
[28] Dowty E and Clark J R 1973 *Z. Kristallogr.* **138** 64
[29] Le Bihan R 1989 *Ferroelectrics* **97** 19